Corrosion Science 235 (2024) 112202

Contents lists available at ScienceDirect

Corrosion Science

journal homepage: www.elsevier.com/locate/corsci

An electrochemical study of iron carbonate layers formed on carbon steel during corrosion in elevated pressure CO_2 environments

Robert Jacklin [a,*], Joshua Owen [a], Amber Sykes [a], Danny Burkle [b], Richard C. Woollam [a], Richard Barker [a]

[a] Institute of Functional Surfaces, School of Mechanical Engineering, University of Leeds, Leeds LS2 9JT, United Kingdom
[b] LBBC Baskerville, Beechwood Street, Leeds LS28 6PT, United Kingdom

ARTICLE INFO

Keywords:
CO_2 corrosion
Carbon steel
Iron carbonate
Electrochemical Impedance Spectroscopy
Autoclave

ABSTRACT

Iron carbonate ($FeCO_3$) layers influence the electrochemical properties of carbon steel during aqueous corrosion in carbon dioxide–saturated environments. In this study, electrochemical measurements conducted in an autoclave at 80°C and 5 barg are combined with cross-sectional imaging to elucidate interfacial properties of X65 carbon steel at key stages of $FeCO_3$ layer development. The effects of evolving system chemistry are also considered by variation of the X65 surface area to solution volume (A/V) ratio. $FeCO_3$ reduces general corrosion rates through a combination of active site blocking and restriction of mass transport, with resultant layer properties dependent on the A/V ratio.

1. Introduction

Produced fluids encountered in hydrocarbon and geothermal energy extraction are often rich in carbon dioxide (CO_2). CO_2 readily dissolves into an aqueous phase and forms carbonic acid (H_2CO_3). As a weak diprotic acid, H_2CO_3 partially dissociates to form bicarbonate (HCO_3^-) and carbonate (CO_3^{2-}) ions through the protonation of water. Although this acidification process can theoretically lead to aggressive corrosion within carbon steel pipework, a combination of superior mechanical properties, low-cost and availability justify the selection of these materials in many applications [1,2].

Under conditions relevant to the current work, the primary cathodic reaction in the corrosion process is considered to be the direct reduction of H^+ ions [3]. The mechanism for this is electrochemical adsorption of the hydrogen ion on to the steel surface, Eq. (1) followed by electrochemical Eq. (2) or chemical desorption Eq. (3).

$$H^+_{(aq)} + e^- \rightarrow H_{ads} \quad (1)$$

$$H_{ads} + H^+_{(aq)} + e^- \rightarrow H_{2(g)} \quad (2)$$

$$H_{ads} + H_{ads} \rightarrow H_{2(g)} \quad (3)$$

The anodic process can be described by a single overall reaction which is the release of a ferrous ion (Fe^{2+}) into the solution:

$$Fe_{(s)} \rightarrow Fe^{2+}_{(aq)} + 2e^- \quad (4)$$

In practice, carbon steels become protected from CO_2 corrosion by a combination of inhibitors, scale and corrosion products, the most common of which is iron carbonate ($FeCO_3$).

$FeCO_3$ forms when the product of activities of CO_3^{2-} and Fe^{2+} exceeds the solubility limit. As Fe^{2+} is released during the anodic dissolution of steel, surface saturation can vary substantially from that of the bulk environment, promoting $FeCO_3$ precipitation at the steel surface [2,4].

Within the literature, the protective properties of $FeCO_3$ layers have been linked to bulk solution conditions such as pH, temperature and CO_2 partial pressure (pCO_2) [3, 5–7] as well as metallurgical properties of the substrate steel [8–10] all of which affect the precipitation rates and growth behaviour of the crystalline layers. In laboratory experiments, compact and adherent layers of $FeCO_3$ have typically been observed at temperatures above 60 °C and pH above 6 [3,11].

At lower initial pH, highly protective layers of $FeCO_3$ have only been observed when formed at elevated pressures and temperatures using autoclaves [12–16]. This has been attributed to a rapid increase in surface pH and super-saturation of $FeCO_3$ from enhanced corrosion kinetics. This type of experiment is typically performed to simulate stagnated environments where pH evolution is expected, such as condensate within super critical CO_2 applications [17,18], or as a means of accelerated testing [12]. Conclusions related to $FeCO_3$ layers formed on

---

* Corresponding author at: Institute of Functional Surfaces, School of Mechanical Engineering, University of Leeds, Leeds LS2 9JT, United Kingdom.
E-mail address: R.A.Jacklin@leeds.ac.uk (R. Jacklin).

https://doi.org/10.1016/j.corsci.2024.112202
Received 13 March 2024; Received in revised form 15 May 2024; Accepted 8 June 2024

carbon steel in autoclave experiments have typically been made using *ex situ* and/or mass loss techniques, with limited *in situ* electrochemical data available.

Electrochemical techniques, such as Electrochemical Impedance Spectroscopy (EIS), provide more extensive information on the underlying mechanisms for substrate protection by capturing the transient nature of interfacial properties as surface chemistry evolves and $FeCO_3$ layers form [4,19].

A lack of electrochemical data at elevated pressure is attributed to factors such as experimental complexity and difficulty obtaining reliable measurements [20], meaning advanced electrochemical studies on $FeCO_3$ layer growth are predominantly conducted at atmospheric pressure [19, 21–24].

Another challenge in conducting elevated pressure experiments is control over the chemical composition of the system over time. In a fixed volume vessel, solution chemistry can evolve substantially in the early stages of a CO_2 corrosion experiment as H^+ is reduced and Fe^{2+} released into the solution. The buffering capacity of CO_2 can replenish H^+ however the proliferation of Fe^{2+} in the solution will shift the equilibrium speciation, increasing pH [25]. The magnitude of any transition in solution chemistry is relative to the concentration of metal ions that enter the system as well as the starting conditions such as pH, temperature, and ionic strength [7].

A compounding factor is that these conditions also determine the rate at which test specimens will corrode by influencing the kinetics of the corrosion reaction, with the corrosion rate effectively a measure of metal ion flux into the system. Some researchers have attempted to control chemistry evolution in laboratory experiments using ion exchange resins to rebalance the system [26,27] or by complete replenishment of the test fluid [28]. Despite successful implementation at atmospheric pressures, extending these methodologies to a high-pressure system would again add significant complexity and cost. Buffer systems such as acetic acid/acetate offer a simplified approach to stabilise pH, although brine complexity is increased, and effectiveness can vary with target pH [29,30].

Another simple approach to solution chemistry control which is often under-reported in literature is to limit the ratio of exposed metal specimens to solution volume, known as the A/V ratio. Reducing the A/V ratio will decrease the relative amount of Fe^{2+} entering the system. Immersion test standards ASTM G111 [31] and ASTM G31 [32] both provide a general recommendation on maximum A/V ratio for corrosion experiments but there is no systematic approach to establish A/V ratio for a specific set of operating conditions. This has also not been specifically addressed in the scientific literature.

In the current work, $FeCO_3$ formation in a low initial pH (<4) CO_2-saturated aqueous environment is characterised at elevated pressure using electrochemical techniques in combination with surface and through layer analysis to build a detailed picture of the key stages of corrosion product layer development. The consequence of evolving system chemistry is also explored by variation of the A/V ratio, providing an improved understanding of elevated pressure experimental methods.

2. Materials and methods

2.1. Material preparation and A/V configuration

Mass loss specimens and working electrodes were machined from a common pipeline material, American Petroleum Institute (API) 5 L X65 carbon steel. The elemental composition of the stock material was measured using a Rigaku ZSX Primus II Wavelength Dispersive X-ray Fluorescence (WDXRF) spectrometer and reported in Table 1. As carbon is not compatible with this technique its value is taken from manufacturer data. All exposed carbon steel surfaces were wet ground with silicon carbide grit paper up to P600 before being rinsed with acetone and dried prior to experiments.

The area-to-volume (A/V) ratio was adjusted using two different geometries of coupon (used for mass loss measurements) as illustrated in Fig. 1. High A/V experiments contained two cylindrical coupons of 25 mm diameter and 6 mm thickness. For low A/V experiments, the coupons were cut into thirds to produce cylindrical-sector specimens of 25 mm diameter, 6 mm thickness and sector angle of 120°. One sector was used per low A/V experiment. Each mass loss coupon had one 3 mm diameter hole drilled through to enable mounting within the autoclave. A 12 mm diameter X65 working electrode (WE) was included in each experiment with a single 1.13 cm^2 exposed face. The sides of the electrode were coated with high temperature lacquer and protected with Fluorinated Ethylene Propylene shrink wrap while the back face was soldered to Kapton coated copper wire before being sealed with high temperature silicone. The same method was used to fabricate a nickel alloy C-276 counter electrode (CE) also of 12 mm diameter. The total exposed surface area of carbon steel was 7.9 cm^2 and 31 cm^2, giving A/V ratios of 10.5 $cm^2 \cdot L^{-1}$ and 41.4 $cm^2 \cdot L^{-1}$ for low and high A/V experiments, respectively. A 3-electrode cell was completed with a refillable-type, external pressure balanced silver/silver chloride (Ag/AgCl) reference electrode (RE) from Corr Instruments.

2.2. Preparation of chemical environment

The brine solution was prepared by addition of 30 g of high purity sodium chloride (NaCl) ($\geq$ 99 % purity) to 1 L of deionised water in a glass beaker. The solution was stirred on a hotplate during continuous CO_2 sparging at atmospheric pressure and room temperature for a minimum of 2 hours prior to each test to pre-saturate the solution and remove dissolved oxygen. CO_2 was simultaneously flushed through a 1.3 L 316SS-Ti autoclave (LBBC Baskerville) containing mass loss coupons suspended within the vessel using a Polytetrafluoroethylene (PTFE) holder depicted in Fig. 1.

The working and counter electrodes were installed through a high-pressure PTFE seated cable gland. Solution was transferred to the vessel in a closed pumping loop depicted in Fig. 1 with transfer lines pre-purged with CO_2. Once 750 mL of solution was transferred to the autoclave the vessel was charged with CO_2 up to 8 bar gauge pressure for 10 minutes at room temperature to expedite the saturation process. After this period the autoclave was heated on a hotplate to 80 °C. During the heating phase, pressure was regulated down to 5 bar gauge and maintained using a back-pressure regulator fitted downstream of the outlet valve. On reaching target temperature the outlet valve was closed allowing system pressure to evolve naturally and electrochemical measurements were initiated. Initial pH was calculated using the model compiled by Nordsveen et al. [2]. Table 2

2.3. Electrochemical measurements

Measurements were performed using an Ivium Compactstat potentiostat, interfaced through IviumSoft software. To mitigate ground loop disturbances the potentiostat was operated in floating mode by removal of an external grounding bridge on the device. This ensured the only route to ground for the system was through the electrically conductive surface of the hotplate. Measurements of open circuit potential (OCP),

Table 1
Elemental composition of API 5 L X65 carbon steel (wt%).

C	Mn	Ni	Nb	Mo	Si	V	P	S	Cr	Cu	Fe
0.15	1.224	0.08	0.04	0.15	0.34	0.06	0.007	0.012	0.09	0.21	Bal.

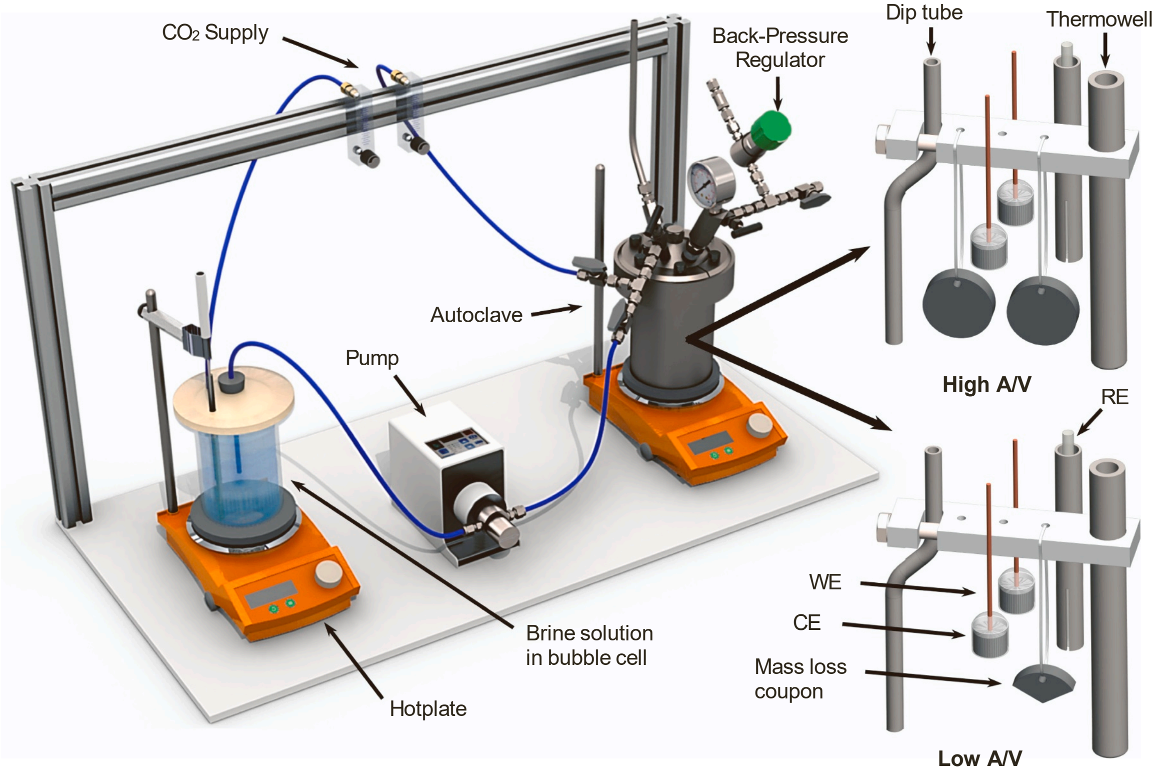

Fig. 1. Experimental apparatus and specimen arrangements for High (41.4 $cm^2 \cdot L^{-1}$) and Low (10.5 $cm^2 \cdot L^{-1}$) A/V ratios.

Table 2
Initial conditions for corrosion experiments.

Experimental Parameter	Units	Value
Specimen Material	-	X65 Carbon Steel
Temperature	°C	80
pCO_2	bar	5.5
Calculated pH	-	3.6
Liquid Volume	mL	750
NaCl	$g \cdot L^{-1}$	30
A/V Ratio	$cm^2 \cdot L^{-1}$	10.5, 41.4

linear polarisation resistance (LPR) and EIS were taken throughout the experiments in a 2-hour loop cycle comprising five LPR measurements and one EIS spectra. LPR measurements were conducted across a potential range of −15 mV to +15 mV vs OCP at a scan rate of 0.25 $mV \cdot s^{-1}$. EIS measurements were acquired at a ±15 mV amplitude through a frequency range of 20 kHz to 10 mHz with 10 frequencies per decade (64 measurements per scan). Potentiodynamic sweeps were performed at the end of one experiment for each A/V ratio. The working electrode was polarized cathodically from +15 mV to −250 mV vs OCP. The electrode was left to stabilise back to its pre-polarisation potential before anodic polarisation from −15 mV to +250 mV vs OCP at a rate of 0.5 $mV \cdot s^{-1}$. Stabilisation period between sweeps was approximately 30 minutes for $FeCO_3$ coated specimens.

2.4. Extraction of corrosion layer properties from impedance data

System parameters, such as charge-transfer resistance (R_{ct}), were estimated by fitting the modelled response of an Equivalent Electrical Circuit (EEC) to the raw data. Despite notable efforts, across the literature [10, 19, 21, 33–35] there is a lack of consistency in the EEC selection which makes comparison of circuit parameters difficult. The most methodical and substantive approach to applying EIS is to prioritise graphical and physical interpretation to justify circuit fitting. As a result, a robust set of parameters can be obtained, allowing straightforward comparisons to be made on the properties of similar corrosion product layers.

The procedure for extraction of impedance data is provided in Fig. 2. Data was first assessed by Kramer Kronig (KK) analysis to verify system stability, remove erroneous data points and establish if measurements settings were appropriate. Raw impedance data was then evaluated alongside corrosion layer surface and cross-sectional images to establish an appropriate EEC that represented the physical system. Regression analysis was performed using MATLAB with impedance expressions coded using the Symbolic Math Toolbox. Initial parameter estimates were obtained graphically and compiled into an initialisation vector. The circuit model expression was converted to a MATLAB function and fitted to the real and imaginary impedance data using a non-linear least squares curve fitting routine (Lsqcurvefit).

By default, Lsqcurvefit utilizes a Trust-Region-Reflective algorithm which enables boundary conditions to be applied if necessary (such as on dispersion coefficients which are bounded to values between 0 and 1). The fitting routine is highly sensitive to the initial value of each parameter and a reasonable first guess for each component is therefore imperative. Where data was too noisy or difficult to interpret using the graphical approach, the initial guess was based on the previous fit.

2.5. Ex situ analysis

Surface morphology and cross-sections were imaged using a Hitachi TM3030Plus Scanning Electron Microscope (SEM) with accelerating voltage of 15 kV and back scattered electron image signal. Elemental analysis Electron Back Scattered Diffraction (EBSD) were conducted on an FEI Quanta 650: FEGESEM environmental SEM with Oxford Instruments INCA 350 EDX system/80 mm X-Max SDD detector, EBSD and KE Centaurus EBSD system. Pixel resolution for mapping was between 0.3 and 0.5 μm. A Bruker D8 X-ray diffractometer was used for crystalline phase identification across a 2θ scan range of 20–70 °, step size of 0.016 ° and scan rate of 0.02 $° s^{-1}$.

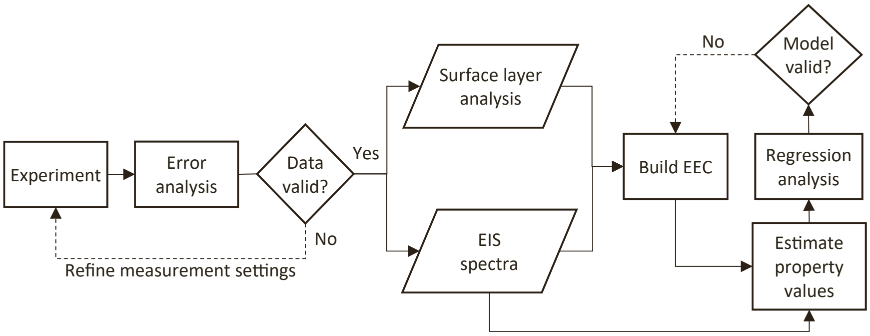

Fig. 2. Flow diagram outlining EIS analysis procedure.

3. Results

3.1. Electrochemical measurements

Results of LPR and OCP measurements at high and low A/V ratio are compared in Fig. 3. The reciprocal of polarisation resistance (R_p^{-1}), analogous to corrosion rate, is plotted as a function of time on a linear and $\log_{10}$ scale to clearly elucidate stages of $FeCO_3$ formation (confirmed as $FeCO_3$ by XRD and shown in the Supplementary Material). On the linear scale, results are shown as an average of R_p^{-1}, with error bars representing the maximum and minimum results from a minimum of two experiments. Four distinct stages of corrosion layer development are evident in Fig. 3, with the end of each stage indicated S1 to S4. During the first stage, corrosion rates are high and relatively stable as OCP gradually increases. In the second stage, corrosion rates begin to drop linearly as OCP dips, indicative of $FeCO_3$ nucleation on the steel surface [36].

In the third stage, corrosion rates begin to reduce logarithmically as OCP increases. Corrosion rates and OCP eventually stabilise in the fourth stage. During the early stage of free corrosion R_p^{-1} appear slightly higher at low A/V. The induction time for $FeCO_3$ nucleation also reduces at high A/V while the rate of decrease in R_p^{-1} in the second and third stages is also slightly enhanced. Although final corrosion rates are comparably low for both A/V ratios, the OCP becomes significantly higher at low A/V by the final stages of the experiment.

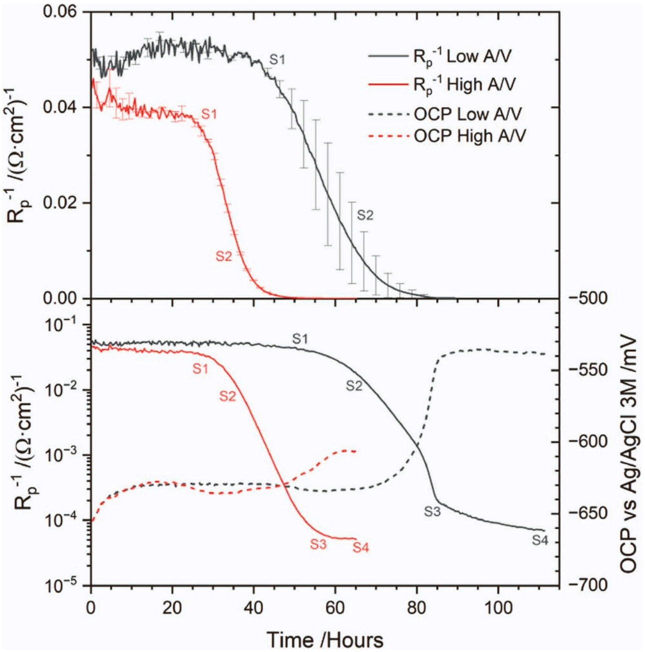

Fig. 3. Comparison of LPR and OCP trends over time for low and high (10.5 and 41.4 $cm^2 \cdot L^{-1}$) A/V ratio experiments on X65 steel in 30 $g \cdot L^{-1}$ NaCl CO_2 solution at 80 °C, 5.5 bar pCO_2 (a) Rp^{-1} on linear scale (b) Rp^{-1} on $\log_{10}$ scale compared with OCP.

Potentiodynamic sweeps in Fig. 4, conducted at the end of the first repeat of each experiment, illustrate differences in anodic and cathodic behaviour between the two layers.

Despite a more positive OCP at low A/V, corrosion current density (i_{corr}) is marginally higher compared with high A/V. This effect is predominately attributed to the suppression of the cathodic branch of the potential curve at high A/V. Conversely, the anodic reaction appears more restricted at low A/V. Fitted impedance spectra for each of the four stages of $FeCO_3$ development are provided in Fig. 5. Despite a higher rate of change in the impedance modulus at high A/V, the Nyquist plots are comparable for the first three stages of $FeCO_3$ development. The impedance response shows three distinct relaxation processes attributed to the following physical phenomena.

3.2. Charge-transfer kinetics

Charge-transfer kinetics are observed within the high frequency region of the impedance spectra, presenting a capacitive loop on a Nyquist plot and modelled by a charge-transfer resistance (R_{ct}) in parallel with the double layer capacitance (C_{dl}). A shift in the semi-circular profile along the real axis is associated with ohmic potential drops that occur across the electrolyte (R_e). The characteristic frequency (ω_c) is located at the minima of Z_{im} (maxima on a plot of $-Z_{im}$) for the high frequency loop. In this system, heterogeneity of the reacting (active) surface gives rise to a dispersion of time constants over the interface. A typical surface distribution creates a depression in the semi-circular profile without distorting the curvature and can be modelled using a constant phase element (CPE) in place of a standard capacitive element. Eq. (5) gives the measured double layer capacitance (Q_{dl}) due to time constant

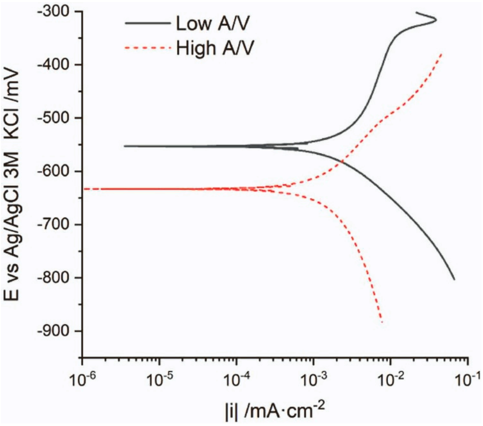

Fig. 4. Polarisation curves for low and high (10.5 and 41.4 $cm^2 \cdot L^{-1}$) A/V ratio experiments on X65 steel in 30 $g \cdot L^{-1}$ NaCl CO_2 solution at 80 °C, 5.5 bar pCO_2.

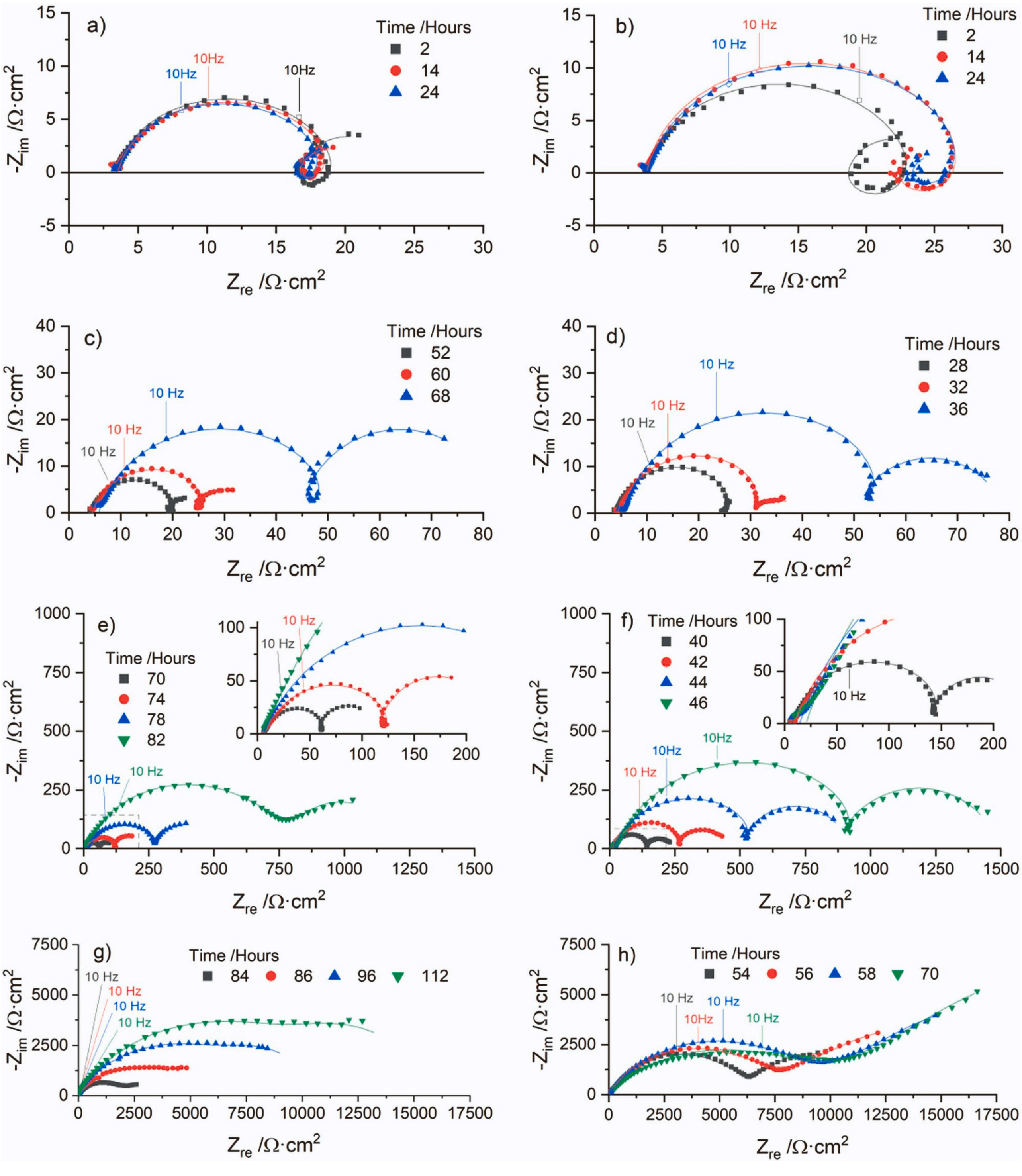

Fig. 5. Nyquist plots to compare impedance response of X65 steel at different stages of $FeCO_3$ formation in 30 $g\cdot L^{-1}$ NaCl CO_2 solution at 80 °C, 5.5 bar pCO_2. (a), (c), (e), (g) Low (10.5 $cm^2\cdot L^{-1}$) A/V ratio. (b), (d), (f), (h) High (41.4 $cm^2\cdot L^{-1}$) A/V ratio.

dispersion, where α is the dispersion coefficient between 0 and 1.

$$Q_{dl} = \frac{1}{\omega_c{}^{\alpha} R_{ct}} \tag{5}$$

The formula of Brug et al. [37] (Eq. 6) has largely been applied to systems with apparent surface distributed properties to establish a true C_{dl} value from Q_{dl} measured and factors in the contribution of R_e to the observed behaviour [38]:

$$C_{dl,surf} = Q_{dl}{}^{1/\alpha}\left(\frac{R_e R_{ct}}{R_e + R_{ct}}\right)^{(1-\alpha)/\alpha} \tag{6}$$

Where $C_{dl,surf}$ distinguishes that the effective double layer capacitance is valid when the time constant is surface distributed.

3.3. *Adsorption*

Bockris et al. [39] described a 'consecutive mechanism' for the anodic dissolution of iron in strong acids, which has often been found to be in good agreement with polarisation behaviour observed from carbon steels in CO_2 saturated environments. The process involves the reaction of Fe with water to form an adsorbed intermediary $(FeOH)_{ads}$ Eqs. (7)-(9).

$$Fe_{(s)} + H_2O_{(l)} \rightleftharpoons (FeOH)_{ads} + H^+_{(aq)} + e^- \tag{7}$$

$$(FeOH)_{ads} \rightarrow FeOH^+_{(aq)} + e^- \tag{8}$$

$$FeOH^+_{(aq)} + H^+_{(aq)} \rightleftharpoons Fe^{2+}_{(aq)} + H_2O_{(l)} \tag{9}$$

This adsorption process has widely been adopted to explain inductive behaviour (L_{ads}) observed in impedance spectra [10, 33, 34, 40–50] including CO_2 corrosion studies at low pH and elevated pCO_2 [33,34,49, 50]. Some studies [51,52] suggest dissolved CO_2 may also be directly involved in the anodic reaction, but the mechanism has not been definitively revealed [53]. This inductive behaviour was also observed in the current study and for the purpose of circuit fitting can be modelled as a parallel combination of an inductor (L_{ads}) and resistance (R_{ads}).

3.4. Diffusion

In the final stage (Fig. 5(g) and (h)) the impedance responses become clearly distinguishable as the high A/V system starts to become dominated by diffusion, exhibiting the typically linear diffusion tail in the low frequency region. When a layer forms on the surface of the electrode it acts as a diffusion barrier which behaves as a transmissive boundary if electroactive species exchange occurs with the bulk electrolyte. In practice, a porous $FeCO_3$ layer may behave as a transmissive boundary diffusion layer, but non-uniform diffusion and the existence of multiple transport pathways can alter the response of the layer in impedance measurements [54–56]. The generalised (fractal) Warburg model was devised applying distributive effects of a Constant Phase Element (CPE) to that of diffusion. Eq. (10) is the fractal Warburg model for a transmissive boundary with dispersion [56,57]:

$$Z_{O_G} = \frac{R_W}{\left(\sqrt{j\omega\tau_D}\right)^{\phi_W}} \tanh\left(\sqrt{j\omega\tau_D}\right)^{\phi_W} \tag{10}$$

where ϕ_W is the exponent ≤ 1 comparable to α in a CPE. R_W is the limiting diffusion resistance as a function of the concentration of mobility and τ_D is the diffusion time constant.

Based on impedance response and SEM images of the current system, the low frequency relaxation process is attributed to transmissive diffusion effects. The initial value of τ_D has been estimated from the local minima of the imaginary impedance against frequency (ω_{min}) according to Eq. (11) derived by Cruz-Manzo and Greenwood [58]:

$$\omega_{min} = \frac{2.54}{2 \cdot \pi \cdot \tau_D} \tag{11}$$

where ω_{min} is in units of Hz.

3.5. Equivalent electrical circuit (EEC)

During the early stages of every experiment there is evidence of three distinct time constants. The first is the high frequency capacitive loop associated with charge transfer kinetics. The second is the inductive behaviour that has previously been attributed to an adsorption process. The third relaxation process, most clearly evident after corrosion product starts to form, is attributed to transmissive mass transport diffusion. Evidence of diffusion impedance from the start of the experiment could be an artefact of slow migration of species to and from the steel surface, as a consequence of high initial corrosion rates and a lack of fluid stirring. The system is modelled using a Randles circuit with a generalised finite length Warburg diffusion element and a parallel combination of an inductor and resistor to model the adsorption profile. The resulting impedance formula is given in Eq. (12) with the equivalent circuit provided in Fig. 6(a).

$$Z = R_e + \frac{1}{\left(R_{ct} + \left(R_{ads}^{-1} + L_{ads}^{-1}\right)^{-1} + Z_{O_G}\right)^{-1} + (j\omega)^{\alpha} Q_{dl}} \tag{12}$$

At the later stages of the experiments the inductive loop is no longer evident and is therefore removed from the model giving Eq. (13) and circuit model Fig. 6(b).

$$Z = R_e + \frac{1}{\left(R_{ct} + Z_{O_G}\right)^{-1} + (j\omega)^{\alpha} Q_{dl}} \tag{13}$$

The reciprocal sum of fitted resistivity parameters, R_{ct}, R_W and R_e obtained from EIS measurements are compared with total polarisation resistance R_p from LPR in Fig. 7(a). The data shows excellent agreement between the two sources of polarisation resistance, particularly in the second and third stages of the experiments where the quality of impedance fits were high due to well defined time constants. Fig. 7(b) provides a breakdown of R_{ct} and R_W over time with both resistances increasing concomitantly throughout the experiments. As indicated in Fig. 5, the final stage of $FeCO_3$ development is where the most notable discrepancies occur between high and low A/V ratio experiments. R_{ct} appears to be greater at low A/V while high A/V has a much higher R_W.

Fig. 8(a) provides a comparison of Q_{dl} behaviour over time. The data follows the same trends observed in resistance measurements however Q_{dl} appears to reduce more significantly at high A/V. To investigate the effects of time constant dispersion, a plot of α and ϕ_W at low and high A/V is provided in Fig. 8(b). At low A/V, ϕ_W generally regressed to a value of 1 during fitting and so has been omitted from the plot. At high A/V ϕ_W could be reliably fitted without bounds due to the clear linearity of the diffusion tail and has also been included in Fig. 8(b). The results show that α is relatively stable at low A/V prior to $FeCO_3$ development, gradually reducing from a value of 0.9–0.7 by the end of the experiment and stabilising during the final stage of the experiment (85–112 hours). At high A/V, α starts decreasing linearly between 24 and 50 hours then starts to drop more sharply between 50 and 70 hours reaching a value of almost 0.54. Diffusion dispersion at high A/V also appears to increase in the later stages of the experiment as the characteristic 45° line of the Warburg element is clearly depressed to a lower angle in this system. The result is a decay in ϕ_W to a value of approximately 0.78.

Active surface area and effective double layer capacitance (C_{dl}) are provided in Fig. 9(a) for the low A/V experiment. These parameters provide a physically meaningful understanding of how the electrochemical reactions change the interfacial properties at the steel surface. As the corrosion process proceeds, the physical surface area available for electrochemical reactions changes. The active surface area (Eq. 14) can be estimated from the ratio of the effective double layer capacitance at the beginning of the experiment to that determined at time t:

$$\%S_a(t) = \frac{C_{dl}(t)}{C_{dl}(0)} \times 100 \tag{14}$$

This relationship assumes that any change in C_{dl} is directly attributable to changes in effective area and not due to other factors such as

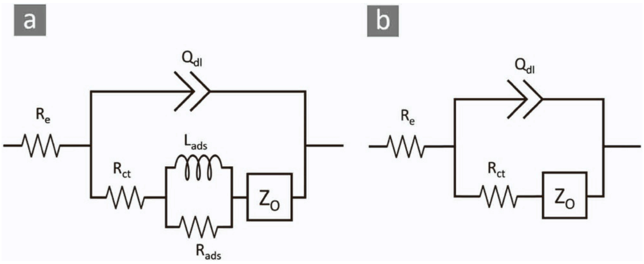

Fig. 6. Selected EEC Models for impedance data fitting.

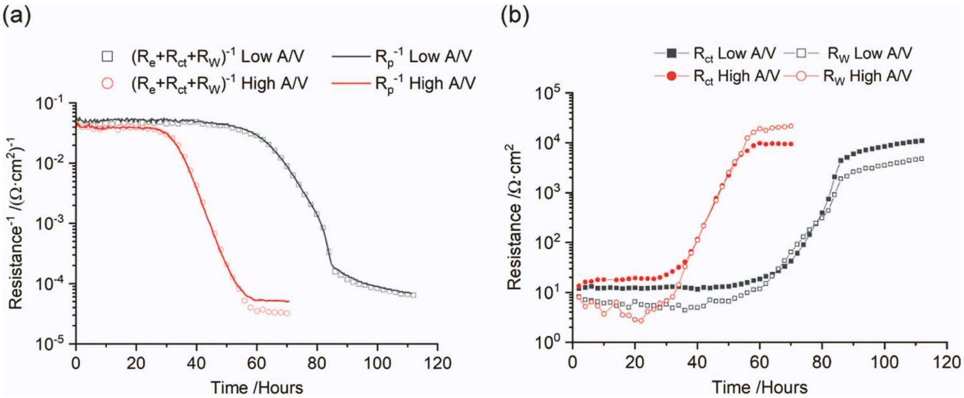

Fig. 7. Resistivity measurements over time (a) Reciprocal sum of resistances (R_e, R_{ct}, R_W) obtained from EIS data fitting compared against R_p^{-1} obtained from LPR measurements (b) Comparison of R_{ct} and R_W from EIS.

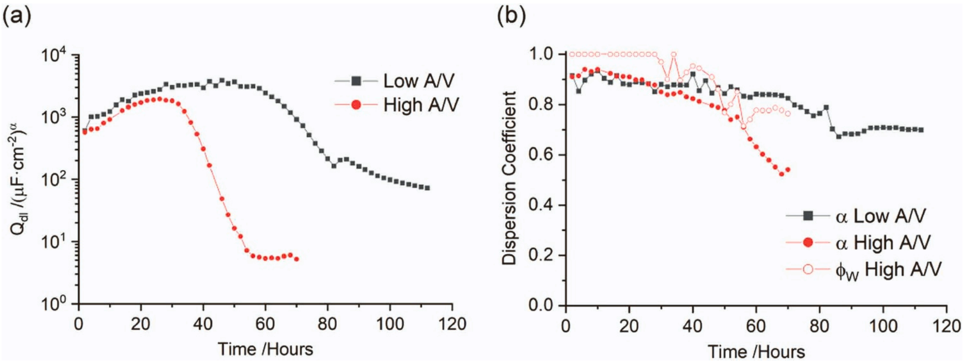

Fig. 8. CPE properties over time for low and high (10.5 and 41.4 $cm^2·L^{-1}$) A/V ratio experiments on X65 steel in 30 $g·L^{-1}$ NaCl CO_2 solution at 80 °C, 5.5 bar pCO_2. (a) Double layer capacitance (b) Dispersion coefficients.

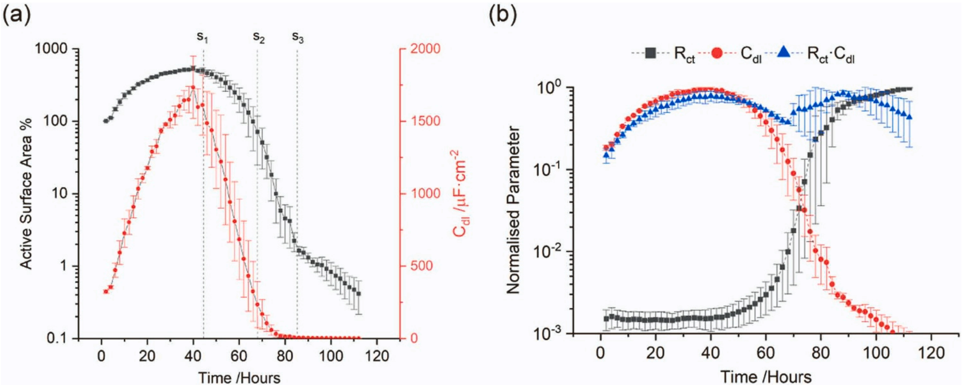

Fig. 9. Evolution of electrochemical properties as $FeCO_3$ corrosion product layer develops on X65 steel in 30 $g·L^{-1}$ NaCl CO_2 solution at 80 °C, 5.5 bar pCO_2 and 10.5 $cm^2·L^{-1}$ A/V ratio.

local chemistry. It has been shown previously that decreasing active surface area decreases double layer capacitance (C_{dl}) and proportionally increases charge transfer resistance R_{ct} [21,59].

The time constant associated with faradaic process $\tau_f = R_{ct}·C_{dl}$ should therefore remain constant while the impedance is controlled by active surface area. When τ_f starts to change it could be an indication that the mechanism controlling the system is also changing.

Initially the active surface area increases, which is aligned with the revealing of the Fe_3C matrix after ferrite depletion. Active surface area begins to decrease as $FeCO_3$ nucleates across the surface, covering reaction sites and slowing down the corrosion process. Fig. 9(b) is a normalised plot showing how the time constant $R_{ct}·C_{dl}$ changes as a result of changes to R_{ct} and C_{dl}. Overall, there is very little change in the time constant from onset of $FeCO_3$ formation to the end of the experiment as both R_{ct} and C_{dl} change with inverse proportionality. This indicates that the system is predominantly controlled by the reduction in active area [21].

3.6. *Ex-situ characterisation*

Comparison of top surface SEM images at the end of high and low A/V experiments in Fig. 10 show a stark contrast in the way in which the corrosion product has formed. Fig. 10 (a) and (c) show a compact and uniform layer of $FeCO_3$ covering the entire surface at high A/V. At low

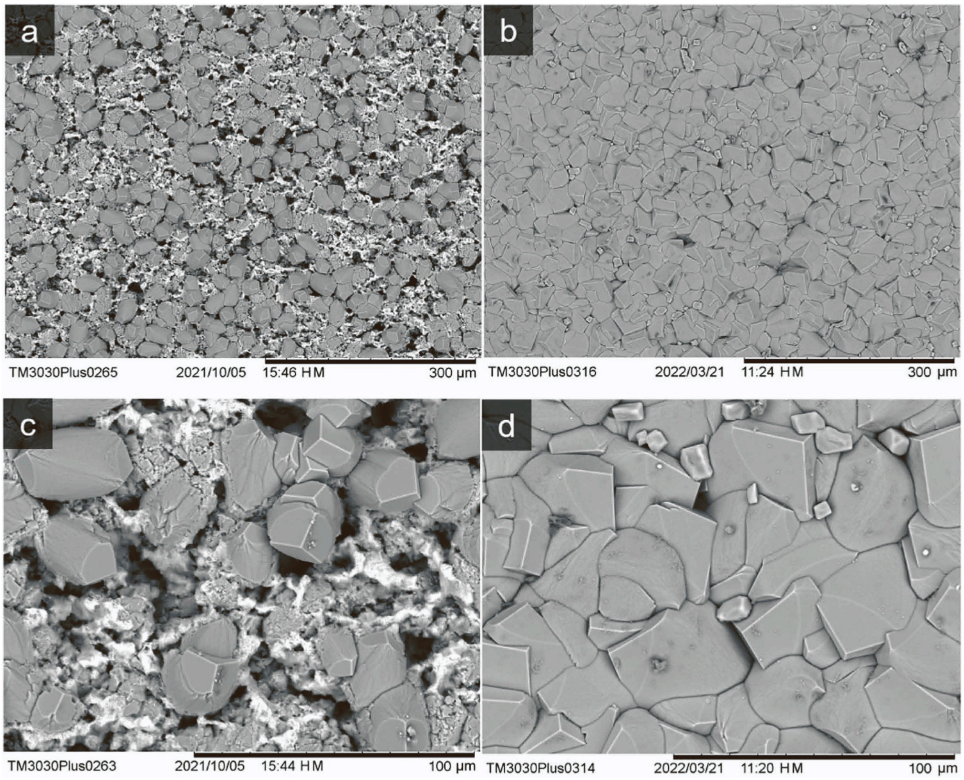

Fig. 10. Back Scatter SEM images of top surface of X65 steel after corrosion product formation in 30 g·L^{-1} NaCl CO_2 solution at 80 °C, 5.5 bar pCO_2. (a) Low A/V 10.5 cm^2·L^{-1} at 250x magnification (b) High A/V 41.4 cm^2·L^{-1} at 250x magnification (c) Low A/V 10.5 cm^2·L^{-1} at 1000x magnification (d) High A/V 41.4 cm^2·L^{-1} at 1000x magnification.

A/V significant Fe_3C (white areas) is still visible at the surface. This could explain the higher cathodic current at low A/V shown in Fig. 4. As a conductive material, Fe_3C is understood to contribute to the cathodic reaction [9]. Cross-sectional SEM images through the corrosion layers in Fig. 11 reveal more detail on the differences in how the layer forms at different A/V ratios. At low A/V the layer thickness is approximately 100 μm and has formed almost entirely within the exposed Fe_3C matrix with only isolated crystals that have grown out and above the original surface. At high A/V the formation is significantly different, comprising an apparent duplex layer of ~40 μm sub-surface $FeCO_3$ embedded into the Fe_3C and a ~20 μm top $FeCO_3$ layer. The apparent duplex layer has been reported previously in literature by Gao *et al.* [60] but it has not been elucidated whether the crystal formation is entirely separate above and below the original surface.

Fig. 12(a) and (b) are images from a forward scatter detector (FSD) which shows contrast between $FeCO_3$ (dark grey) and the ferrite phase from the substrate (light grey/white).

Also visible in these images are the Fe_3C structures within which the $FeCO_3$ is embedded as shown in the SEM images in Fig. 11. Fig. 12(c) and (d) are phase colour images which clearly identify the $FeCO_3$ and body-centre-cubic (BCC) α-ferrite of the substrate but is unable to detect the thin lamella Fe_3C. Fig. 12(e) and (f) are Euler colour images which identify grain boundaries and distinguish crystallographic orientation. All α-ferrite in the Euler images has been recoloured to white to separate them from $FeCO_3$ crystals. EBSD analysis reveals that at high A/V the crystal size is marginally greater than at low A/V. The EBSD data also

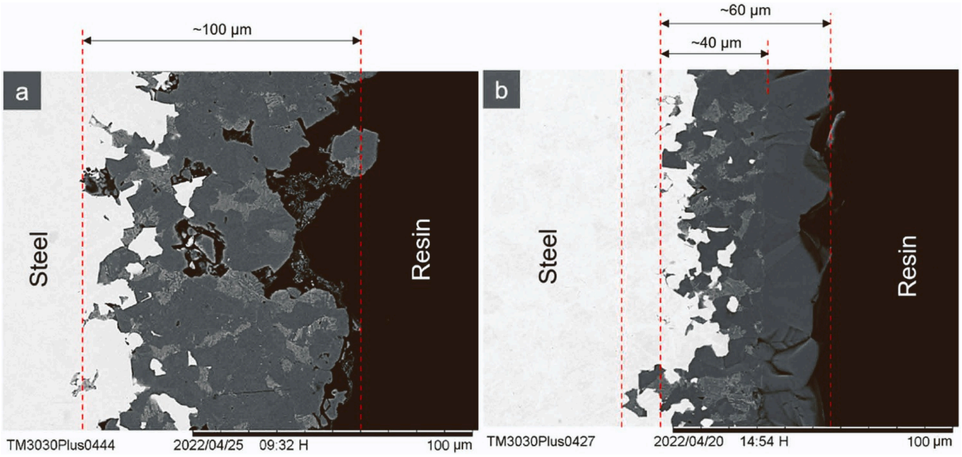

Fig. 11. Back Scattered SEM images of cross section through corrosion product layer on X65 steel after immersion in 30 g·L^{-1} NaCl CO_2 solution at 80 °C, 5.5 bar pCO_2. (a) Low A/V 10.5 cm^2·L^{-1} (b) High A/V 41.4 cm^2·L^{-1}.

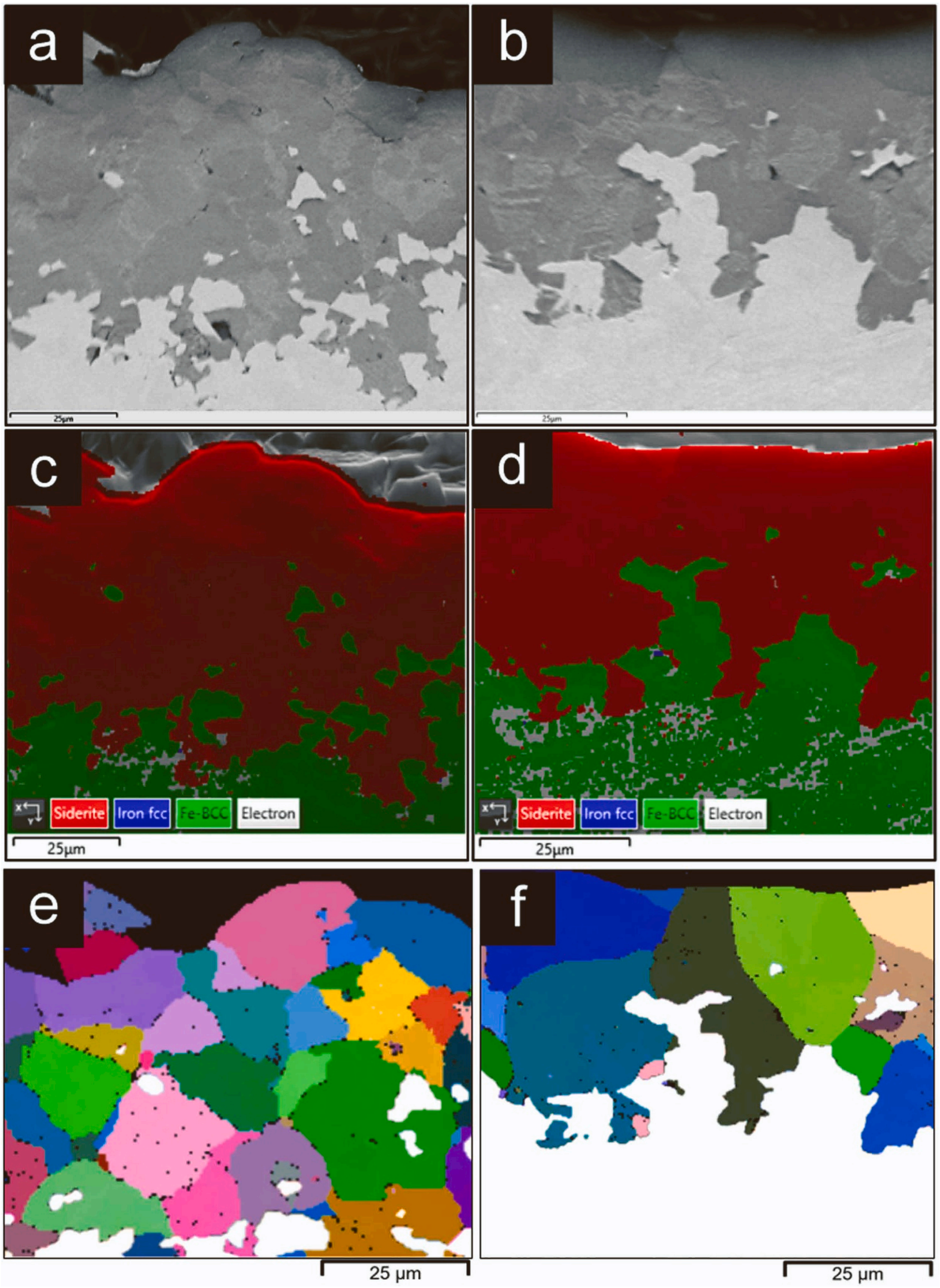

Fig. 12. EBSD images comparing crystal grain structure of $FeCO_3$ products formed at high and low (10.5 and 41.4 $cm^2 \cdot L^{-1}$) A/V ratios on X65 steel in 30 $g \cdot L^{-1}$ NaCl CO_2 solution at 80 °C, 5.5 bar pCO_2. (a) Low A/V forward scatter image (b) High A/V forward scatter image (c) Low A/V phase colour image (d) High A/V phase colour image (e) Low A/V Euler colour image (f) High A/V Euler colour image.

shows that there is no obvious separation of crystals at the interface of the original steel surface. At high A/V multiple large crystals have formed through the entire depth of the corrosion product from the substrate all the way through to the surface. This also highlights that crystal growth does not appear to be bounded by the Fe_3C with crystals growing over the thin Fe_3C lamella.

3.7. XRD

The results of X-ray diffraction are presented in Fig. 13 identifying $FeCO_3$ as the only crystalline phase present.

3.8. Stages of $FeCO_3$ development at Low A/V

Having established differences in corrosion layer properties due to A/V ratio, the low A/V system, more representative of a stable bulk environment, was selected for further investigation on physical parameters. Fig. 14 shows cross-sectional SEM images taken from repeat experiments that were terminated during each stage of $FeCO_3$ development highlighted in Fig. 3.

Fig. 14(a) is the interface at time S1, just as corrosion rate was starting to reduce, and indicates that $FeCO_3$ crystals have started to nucleate on the surface (darker grey areas as verified with EBSD). Approximate steel penetration at this stage was 50 µm from cross-section analysis. The corresponding penetration based on mass loss measurement for the same experiment was 47 µm. The SEM image of the

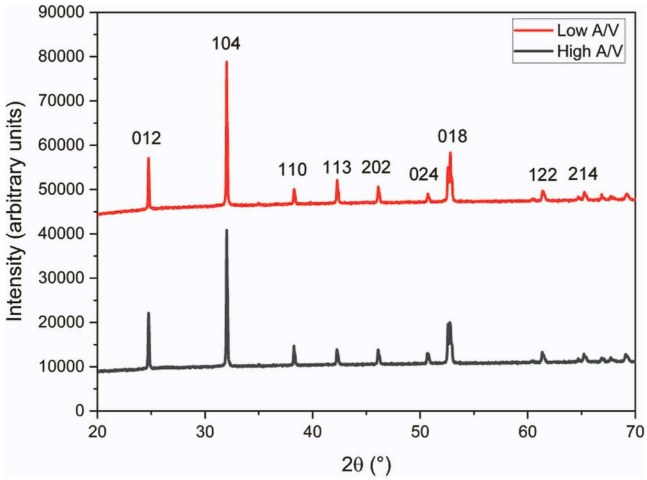

Fig. 13. Powder diffraction patterns identifying crystalline $FeCO_3$ corrosion products after formation at high and low (10.5 and 41.4 $cm^2 \cdot L^{-1}$) A/V ratios on X65 steel in 30 $g \cdot L^{-1}$ NaCl CO_2 solution at 80 °C, 5.5 bar pCO_2. Peak comparison from ICDD Reference data for pure Siderite (00–008–0133).

interface after a 60-hour experiment (Between S1 and S2 in Fig. 3) is shown in Fig. 14(b). At this stage total penetration of the steel has increased to around 76 µm and significant $FeCO_3$ has precipitated within the Fe_3C structure. Noticeably however, there are large gaps between the $FeCO_3$ layer and the steel substrate.

Fig. 14(c) is the interface after 74 hours (Between S2 and S3 in Fig. 3) total penetration of the steel has increased to around 92 µm and the $FeCO_3$ layer has grown further down in to the Fe_3C matrix, leaving smaller, but still visible, voids at the interface with the steel. Other larger voids exist throughout the layer indicating significant porosity may still exist.

A cross-section through the layer that had formed after 112 hours of exposure is shown in Fig. 14(d). At this stage the maximum penetration of the steel is between 100 and 105 µm. Gaps between the substrate and the $FeCO_3$ have largely been filled but significant porosity still exists in the layer which has grown almost entirely within the Fe_3C matrix.

3.9. *Mechanism of substrate protection*

$FeCO_3$ that forms within Fe_3C can only be considered protective when it is able to form directly adjacent to the metal surface [61]. Unprotective layers are said to occur when the $FeCO_3$ forms within the Fe_3C but detached from the substrate. In the current study, at low A/V there is just enough Fe^{2+} in the system to displace that lost from the anodic dissolution with a similar volume of $FeCO_3$ and hence the $FeCO_3$ layer thickness is roughly equal to the steel penetration depth by the end of experiments. Agglomeration of the $FeCO_3$ layer provides a mass transport barrier, preventing further undermining of the layer and allowing gaps at the interface between steel and $FeCO_3$ to be filled, eventually providing substrate protection.

In terms of diffusivity, the change in diffusion resistance is predominantly attributed to an increase in the diffusion length δ_f, with the assumption that diffusion coefficients remain stable. δ_f is related to the tortuosity and overall thickness of the layer, which is shown to increase between stage tests at low A/V. In Fig. 7(b), R_{ct} and R_W increase concomitantly, the explanation for this is that layer thickness increase is dependent on removal of $Fe_{(s)}$ at the surface (Eq. 4) and corresponding production of Fe^{2+} during the anodic reaction to form $FeCO_3$ (Eq. 15).

$$Fe^{2+}_{(aq)} + CO_3{}^{2-} \rightarrow FeCO_3 \tag{15}$$

When the anodic reaction (Eq. 4) becomes suppressed the rate of layer thickness increase is also impeded. The overall stages of $FeCO_3$ development at low A/V can be described as follows and illustrated in Fig. 15:

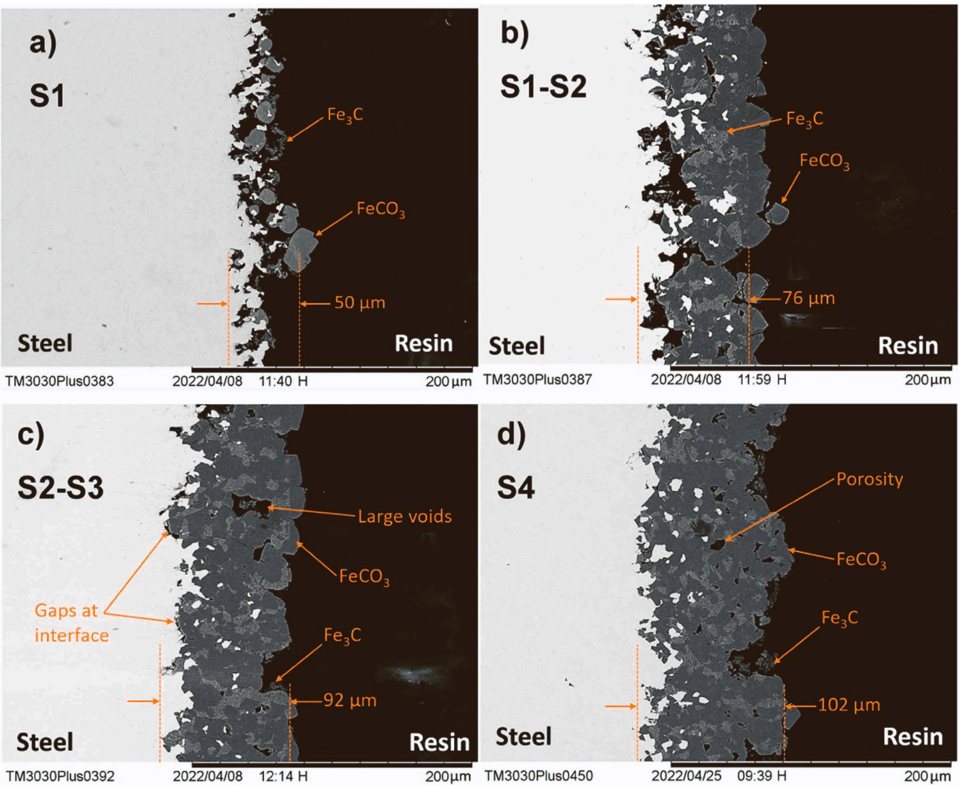

Fig. 14. BSE SEM images of $FeCO_3$ corrosion product development on X65 steel in 30 $g \cdot L^{-1}$ NaCl CO_2 solution at 80 °C, 5.5 bar pCO_2 and 10.5 $cm^2 \cdot L^{-1}$ A/V.

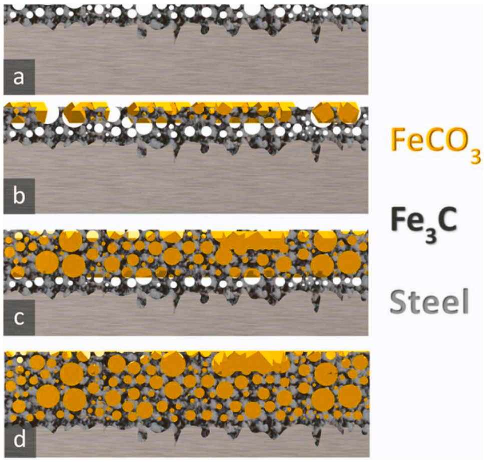

Fig. 15. Proposed $FeCO_3$ growth behaviour at low A/V (a) Revealing of Fe_3C matrix (b) Initial nucleation of $FeCO_3$ (c) Formation of $FeCO_3$ barrier (d) Void filling adjacent to surface.

Stage 1: Active corrosion with preferential dissolution of ferrite exposing an Fe_3C matrix and leading to an increase in active surface area.

Stage 2: Nucleation and growth of $FeCO_3$ crystals within the Fe_3C matrix resulting in a reduction of active surface area and a linear increase in charge transfer resistance.

Stage 3: Convergence of $FeCO_3$ crystals to produce a diffusion barrier with increasing thickness and a logarithmic increase in both charge transfer and diffusion resistance. The corrosion layer thickness increases due to continued undermining of the layer.

Stage 4: Eventually the diffusion layer thickness appears sufficient to limit active specie concentrations and voids between the substrate and $FeCO_3$ are reduced. This process further increases charge transfer resistance whilst also restricting continued corrosion layer growth. The latter results in a reduction in the rate of increase in diffusion resistance as the layer thickness stabilises.

At high A/V the increase in bulk Fe^{2+} led to expedited accumulation of $FeCO_3$ resulting in a corrosion layer thickness greater than steel penetration. This creates a bilayer that forms both within and above the existing Fe_3C structure (Figs. 11 and 16). Visual observations of the layer cross section suggest that the corrosion layer is more densely packed above the Fe_3C providing a more effective diffusion barrier. The heterogeneity of Fe_3C may encourage crystal nucleation while inhibiting growth and agglomeration, resulting in smaller crystallites with greater porosity between crystals. The results have also shown that the two systems do not converge over time due to significant differences in evolution of the layers during the early stages of the experiment when dissolution rates and Fe^{2+} flux is high. The layer thickness at high A/V will likely never reach the same thickness as at low A/V while at low A/V it is unlikely that a thick outer layer will form due to the lack of Fe^{2+} reaching the outer surface. The growth mechanism suggests that microstructure may play a pivotal role in the sensitivity of an experiment to A/V ratio. The presence of an Fe_3C structure in X65 steel not only provides an anchor site for $FeCO_3$ layers [10] but has significant galvanic interaction with bare carbon steel [9]. These properties accentuate the electrochemical differences between the layers formed in the current study.

4. Conclusions

- A combination of direct current (LPR) and alternating current (EIS) techniques have been used in conjunction with electron microscopy imaging through the layer thickness to characterize the formation of $FeCO_3$ on X65 carbon steel at elevated pressure (5.5 bar pCO_2) and temperature (80°C) at unbuffered pH.
- The work enables greater understanding on $FeCO_3$ formation in more demanding CO_2 environments identifying four main stages in layer development.
- This study has also demonstrated that area-to-volume (A/V) ratio has a significant effect on the formation of $FeCO_3$ corrosion products both in terms of the rate of formation and the subsequent morphology and performance of the layer. *In situ* electrochemical measurements indicate that the mechanism for protection of the substrate changes due to the morphology of the layer.
- At high A/V the increased rate of corrosion product formation results in a dense top surface layer of $FeCO_3$ which provides a higher level of diffusion resistance compared to the thicker more porous layer that grows almost entirely within the exposed Fe_3C from the substrate at low A/V.
- Selection of A/V ratio should not only factor the permissible total change in the chemical environment as a consequence of the corrosion process, but also the rate at which the environment changes. This can be achieved by *in situ* electrochemical techniques, such as impedance and pH monitoring.
- This work further reiterates the need for caution when drawing conclusions from laboratory scale experiments, particularly when developing novel techniques for corrosion prevention such as the use of naturally protective corrosion products. Field conditions can vary greatly even within the same system and are often not well defined. A robust and extensive experimental approach is therefore required to confidently translate the true performance of corrosion products from laboratory scale experiments to the field.

CRediT authorship contribution statement

Robert Jacklin: Writing – review & editing, Writing – original draft, Visualization, Methodology, Investigation, Formal analysis, Data curation, Conceptualization. **Joshua Owen:** Writing – review & editing, Supervision, Formal analysis, Methodology, Conceptualization. **Amber Sykes:** Validation, Investigation. **Danny Burkle:** Supervision, Resources, Conceptualization, Funding acquisition. **Richard Woollam:** Writing – review & editing, Supervision, Methodology, Formal analysis. **Richard Barker:** Writing – review & editing, Supervision, Conceptualization, Funding acquisition, Methodology.

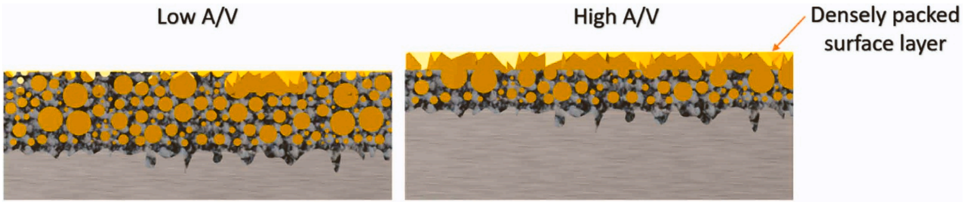

Fig. 16. Comparison of $FeCO_3$ layers formed at low and high A/V.

Declaration of Competing Interest

The authors declare the following financial interests/personal relationships which may be considered as potential competing interests: Robert Jacklin reports financial support was provided by LBBC Baskerville. If there are other authors, they declare that they have no known competing financial interests or personal relationships that could have appeared to influence the work reported in this paper

Data Availability

Data will be made available on request.

Acknowledgements

The authors would like to acknowledge funding from Engineering and Physical Sciences Research Council and LBBC Baskerville. The authors would also like to thank the contribution from Stuart Micklethwaite and Richard Walshaw at University of Leeds Electron Microscopy and Spectroscopy Centre (LEMAS) for completion of SEM and EBSD analysis.

References

[1] M.B. Kermani, A. Morshed, Carbon dioxide corrosion in oil and gas production—a compendium, Corrosion 59 (8) (2003) 659–683.

[2] M. Nordsveen, S. Nešić, R. Nyborg, A. Stangeland, A mechanistic model for carbon dioxide corrosion of mild steel in the presence of protective iron carbonate films—Part 1: theory and verification, Corrosion 59 (5) (2003) 443–456.

[3] R. Barker, D. Burkle, T. Charpentier, H. Thompson, A. Neville, A review of iron carbonate ($FeCO_3$) formation in the oil and gas industry, Corros. Sci. 142 (2018) 312–341.

[4] R. De Motte, et al., Near surface pH measurements in aqueous CO_2 corrosion, Electrochim. Acta 290 (2018) 605–615.

[5] W. Sun, S. Nešić, Kinetics of corrosion layer formation: Part 1—iron carbonate layers in carbon dioxide corrosion, Corrosion 64 (4) (2008) 334–346.

[6] Tomson, M.B. and Johnson, M.L. How Ferrous Carbonate Kinetics Impacts Oilfield Corrosion. In: SPE International Symposium on Oilfield Chemistry, 01/01/1991, Anaheim, California. Society of Petroleum Engineers, 1991, p.8.

[7] Dugstad, A. Fundamental Aspects of CO_2 Metal Loss Corrosion - Part 1: Mechanism. *In: CORROSION 2006*, 12-16 March 2006, San Diego, California. NACE International, 2006, p.18.

[8] A. Dugstad, H. Hemmer, M. Seiersten, Effect of Steel Microstructure on Corrosion Rate and Protective Iron Carbonate Film Formation, in: Corrosion, 57, 2001, pp. 369–378.

[9] J. Owen, F. Ropital, G.R. Joshi, J. Kittel, R. Barker, Galvanic effects induced by siderite and cementite surface layers on carbon steel in aqueous CO_2 environments, Corros. Sci. 209 (2022) 110762.

[10] F. Farelas, M. Galicia, B. Brown, S. Nešić, H. Castaneda, Evolution of dissolution processes at the interface of carbon steel corroding in a CO_2 environment studied by EIS, Corros. Sci. 52 (2) (2010) 509–517.

[11] C. de Waard, U. Lotz, D.E. Milliams, Predictive Model for CO_2 Corrosion Engineering in Wet Natural Gas Pipelines, Corrosion 47 (12) (1991) 976–985.

[12] Y. Hua, A. Shamsa, R. Barker, A. Neville, Protectiveness, morphology and composition of corrosion products formed on carbon steel in the presence of Cl^-, Ca^{2+} and Mg^{2+} in high pressure CO_2 environments, Appl. Surf. Sci. 455 (2018) 667–682.

[13] A. Shamsa, et al., The role of Ca^{2+} ions on Ca/Fe carbonate products on X65 carbon steel in CO_2 corrosion environments at 80 and 150 °C, Corros. Sci. 156 (2019) 58–70.

[14] K. Videm, A. Dugstad, Film covered corrosion, film breakdown and pitting attack of carbon steels in aqueous CO_2 environments, March 21-25 1988, St. Louis, MO. NACE, in: Corrosion, *88*, 1988.

[15] Suhor, M.F., Mohamed, M.F., Nor, A.M., Singer, M. and Nesic, S. Corrosion of Mild Steel in High CO_2 Environment: Effect of the $FeCO_3$ Layer. In: CORROSION *2012*, NACE-2012-1434, 2012.

[16] Gavanluei, A.B., Mishra, B. and Olson, D.L. Corrosion Rate Measurement of a Downhole Tubular Steel at Different CO_2 Partial Pressures and Temperatures and Calculation of the Activation Energy of the Corrosion Process. In: CORROSION 2013, NACE-2013-2298, 2013.

[17] Y. Hua, R. Barker, A. Neville, Comparison of corrosion behaviour for X-65 carbon steel in supercritical CO2-saturated water and water-saturated/unsaturated supercritical CO2, J. Supercrit. Fluids 97 (2015) 224–237.

[18] J.S. de Sá, R. Jacklin, J.A.C.P. Gomes, R. Barker, Formation and protectiveness of Fe/Ca carbonate layer on X80 steel in high-Pressure CO2 corrosion environments, Corrosion 79 (7) (2023) 782–789.

[19] M. Al Kindi, et al., Substrate protection with corrosion scales: can we depend on iron carbonate? ACS Appl. Mater. Interfaces 13 (48) (2021) 58193–58200.

[20] A. Vallejo Vitaller, U.M. Angst, B. Elsener, A setup for electrochemical corrosion testing at elevated temperature and pressure, Measurement 155 (2020) 107537.

[21] R. De Motte, et al., A study by electrochemical impedance spectroscopy and surface analysis of corrosion product layers formed during CO_2 corrosion of low alloy steel, Corros. Sci. 172 (2020) 108666.

[22] A. Lazareva, J. Owen, S. Vargas, R. Barker, A. Neville, Investigation of the evolution of an iron carbonate layer and its effect on localized corrosion of X65 carbon steel in CO_2 corrosion environments, Corros. Sci. 192 (2021) 109849.

[23] G.R. Joshi, et al., Temporal evolution of sweet oilfield corrosion scale: phases, morphologies, habits, and protection, Corros. Sci. 142 (2018) 110–118.

[24] D. Burkle, et al., In situ SR-XRD study of $FeCO_3$ precipitation kinetics onto carbon steel in CO_2-containing environments: The influence of brine pH, Electrochim. Acta 255 (2017) 127–144.

[25] A. Kahyarian, S. Nešić, A new narrative for CO2 corrosion of mild steel, J. Electrochem. Soc. 166 (11) (2019) C3048–C3063.

[26] H. Mansoori, D. Young, B. Brown, S. Nesic, M. Singer, Effect of $CaCO_3$-saturated solution on CO_2 corrosion of mild steel explored in a system with controlled water chemistry and well-defined mass transfer conditions, Corros. Sci. 158 (2019) 108078.

[27] H. Mansoori, B. Brown, D. Young, S. Nešić, M. Singer, Effect of $Fe_xCa_yCO_3$ and $CaCO_3$ Scales on the CO_2 Corrosion of Mild Steel, Corros. J. 75 (12) (2019) 1434–1449.

[28] S. Ieamsupapong, B. Brown, M. Singer, S. Nešić, Effect of Solution pH on Corrosion Product Layer Formation in a Controlled Water Chemistry System. CORROSION 2017, 26-30 March 2017, NACE International, New Orleans, Louisiana, USA, 2017.

[29] Thébault, F., Gomes, C., Pennequin, J. and Marchebois, H. Means and Consequence of pH Control for the Qualification of OCTG Sour Service Grades. *In:* CORROSION 2021, 19-30 April, Virtual. NACE International, 2021.

[30] Crolet, J.L. and Jean Leyer, J.L. Use and Abuse of Artificial Acetate Buffering in Standardized and Application Specific Testing. *In: CORROSION 2004*, 28 March - 1 April, New Orleans, Louisiana, USA. NACE International, 2004.

[31] ASTM International. ASTM G111-21A, Standard Guide for Corrosion Tests in High Temperature or High Pressure Environment, or Both, ASTM International, 2021.

[32] ASTM International. ASTM G31-21, Standard Guide for Laboratory Immersion Corrosion Testing of Metals, ASTM International, West Conshohocken, PA, 2021.

[33] C. Wang, et al., Anti-corrosion characteristics of $FeCO_3$ and $Fe_xCa_yMg_zCO_3$ scales on carbon steel in high-PT CO_2 environments, Chem. Eng. J. 431 (2022) 133484.

[34] J. Chen, X. Wang, H. Ma, Z. Huo, Y. Wang, Experimental Investigation on Corrosion Behavior of X80 Pipeline Steel under Carbon Dioxide Aqueous Conditions, ACS Omega 7 (7) (2022) 6142–6150.

[35] K. Gao, et al., Mechanical properties of CO_2 corrosion product scales and their relationship to corrosion rates, Corros. Sci. 50 (10) (2008) 2796–2803.

[36] J. Owen, et al., In situ SR-XRD analysis of corrosion product formation during 'pseudo-passivation' of carbon steel in CO_2-containing aqueous environments, Corros. Sci. 225 (2023) 111598.

[37] G.J. Brug, A.L.G. van den Eeden, M. Sluyters-Rehbach, J.H. Sluyters, The analysis of electrode impedances complicated by the presence of a constant phase element, J. Electroanal. Chem. Interfacial Electrochem. 176 (1) (1984) 275–295.

[38] M.E. Orazem, B. Tribollet. Electrochemical Impedance Spectroscopy, 2nd ed., John Wiley & Sons, 2017.

[39] J.O.M. Bockris, D. Drazic, A.R. Despic, The electrode kinetics of the deposition and dissolution of iron, Electrochim. Acta 4 (2) (1961) 325–361.

[40] I. Epelboin, M. Keddam, Faradaic Impedances: Diffusion Impedance and Reaction Impedance, J. Electrochem. Soc. 117 (8) (1970) 1052.

[41] B. Bechet, I. Epelboin, M. Keddam, New data from impedance measurements concerning the anodic dissolution of iron in acidic sulphuric media, J. Electroanal. Chem. Interfacial Electrochem. 76 (1) (1977) 129–134.

[42] M. Keddam, O.R. Mottos, H. Takenouti, Reaction Model for Iron Dissolution Studied by Electrode Impedance: I. Experimental Results and Reaction Model, J. Electrochem. Soc. 128 (2) (1981) 257–266.

[43] M. Keddam, O.R. Mattos, H. Takenouti, Reaction Model for Iron Dissolution Studied by Electrode Impedance: II. Determination of the Reaction Model, J. Electrochem. Soc. 128 (2) (1981) 266–274.

[44] O.E. Barcia, O.R. Mattos, The role of chloride and sulphate anions in the iron dissolution mechanism studied by impedance measurements, Electrochim. Acta 35 (6) (1990) 1003–1009.

[45] P. Li, T.C. Tan, J.Y. Lee, Impedance spectra of the anodic dissolution of mild steel in sulfuric acid, Corros. Sci. 38 (11) (1996) 1935–1955.

[46] G. Zhang, C. Chen, M. Lu, C. Chai, Y. Wu, Evaluation of inhibition efficiency of an imidazoline derivative in CO_2-containing aqueous solution, Mater. Chem. Phys. 105 (2) (2007) 331–340.

[47] G.A. Zhang, Y.F. Cheng, On the fundamentals of electrochemical corrosion of X65 steel in CO_2-containing formation water in the presence of acetic acid in petroleum production, Corros. Sci. 51 (1) (2009) 87–94.

[48] T. Tanupabrungsun, B. Brown, S. Nešić, Effect of pH on CO_2 Corrosion of Mild Steel at Elevated Temperatures. *CORROSION 2013*, 17-21 March 2013, NACE International, Orlando, Florida, 2013, p. 11.

[49] Almeida, T.C., Mattos, O.R., Bandeira, M.C.E. and Moreira, R.M. The Effect of High Partial Pressure of CO_2 on the Corrosion Mechanism of Carbon Steel in H_2O-CO_2 Systems. *In: CORROSION 2018*, NACE-2018-11623, 2018.

[50] S. Li, Z. Zeng, M.A. Harris, L.J. Sánchez, H. Cong, CO_2 Corrosion of Low Carbon Steel Under the Joint Effects of Time-Temperature-Salt Concentration, Front. Mater. 6 (2019).

[51] D.M. Dražić, Iron and Its Electrochemistry in an Active State, in: B.E. CONWAY, J. O.M. BOCKRIS, R.E. WHITE (Eds.), Modern Aspects of Electrochemistry, Springer US, Boston, MA, 1989, pp. 69–192.

[52] S. Nešić, N. Thevenot, J.L. Crolet, D. Drazic, Electrochemical Properties of Iron Dissolution in the Presence of CO_2 - Basics Revisited. *CORROSION 96*, 24-29 March 1996, NACE International, Denver, Colorado, 1996, p. 23.

[53] T. das Chagas Almeida, M.C.E. Bandeira, R.M. Moreira, O.R. Mattos, New insights on the role of CO_2 in the mechanism of carbon steel corrosion, Corros. Sci. 120 (2017) 239–250.

[54] A. Lasia, Electrochemical impedance spectroscopy and its applications, Springer, New York, 2020.

[55] Barsoukov, E. and Macdonald, J.R. *Impedance spectroscopy: theory, experiment, and applications.* Second edition / edited by Evgenij Barsoukov, J. Ross Macdonald. ed. Hoboken, N.J.: Wiley-Interscience, 2005.

56] B.A. Boukamp, Derivation of a Distribution Function of Relaxation Times for the (fractal) Finite Length Warburg, Electrochim. Acta 252 (2017) 154–163.

[57] T.Q. Nguyen, C. Breitkopf, Determination of Diffusion Coefficients Using Impedance Spectroscopy Data, J. Electrochem. Soc. 165 (14) (2018) E826–E831.

[58] S. Cruz-Manzo, P. Greenwood, Frequency Transition from Diffusion to Capacitive Response in the Blocked-Diffusion Warburg Impedance for EIS Analysis in Modern Batteries, J. Electrochem. Soc. 167 (14) (2020) 140507.

[59] O. Devos, C. Gabrielli, B. Tribollet, Simultaneous EIS and in situ microscope observation on a partially blocked electrode application to scale electrodeposition, Electrochim. Acta 51 (8) (2006) 1413–1422.

[60] M. Gao, X. Pang, K. Gao, The growth mechanism of CO_2 corrosion product films, Corros. Sci. 53 (2) (2011) 557–568.

[61] J.L. Crolet, N. Thevenot, S. Nesic, Role of conductive corrosion products in the protectiveness of corrosion layers, Corrosion 54 (3) (1998) 194–203.